

ANALYSIS OF THE AERODYNAMIC LOADS ON A WIND TURBINE IN OFF-DESIGN CONDITIONS

G. Santo^{1*}, M. Peeters², W. Van Paepegem² and J. Degroote^{1,3}

¹ Department of Flow, Heat and Combustion Mechanics, Ghent University
Sint-Pietersnieuwstraat 41 – 9000 Ghent, Belgium
{gilberto.santo; joris.degroote}@ugent.be

² Department of Materials Science and Engineering, Ghent University,
Technologiepark-Zwijnaarde 903 - 9052 Zwijnaarde, Belgium
{mathijs.peeters; wim.vanpaepegem}@ugent.be

³ Flanders Make, Belgium

Key Words: *Wind energy, Aerodynamics, Turbulence, Overset.*

Abstract. In this work, the aerodynamic loads acting on a large horizontal axis wind turbine are analysed in off-design conditions by means of computational fluid dynamics (CFD) simulations.

The turbulent wind flow is solved using an unsteady RANS approach and choosing the *k-epsilon* model. The inlet conditions first proposed by Richard and Hoxey are imposed in order to include the atmospheric boundary layer (ABL) profiles for turbulence and velocity at the inlet of the computational domain. Modified wall functions are employed on the ground wall in order to preserve the ABL profiles throughout the entire domain.

A structured background mesh is used. Several component meshes, reproducing the blades and the supporting structures (tower and nacelle), are overlapped and connected to the background mesh by means of an overset technique. The connectivity is then updated every time step to follow the rotation of the wind rotor.

Changing both the pitch angle of the blades and the tip-speed ratio (TSR) of the turbine, several operating points are investigated. The performance and the loads are highly affected by the ABL, whose effect is highlighted. The performance of the wind turbine in each simulated operating point is compared to the nominal operating point (NOP). The aerodynamic loads are monitored, analysed and mutually compared throughout the motion of the rotor in order to identify the most critical conditions for the blade structures.

1 INTRODUCTION

In the last decades, large efforts have been made to explore alternative techniques to replace fossil fuels as energy source. In particular, among renewable energies, wind energy plays an increasingly important role. Given the aleatory nature of the wind, wind turbines are designed to function in a wide range of operating conditions [1]. For this reason, their operation has to be adapted to face the incoming wind and adapt the output power accordingly. Normally, in large horizontal axis wind turbines, this is achieved by pitching the blades (i.e. rotating them around their own axes) and/or changing the tip speed ratio. These controlling techniques can be investigated in detail by mean of computational fluid dynamics (CFD). Sudhamshu et al. [2] carried out CFD (steady RANS) simulations of the NREL Phase VI wind turbine, modelling only one blade and changing both the incoming constant wind speed and the blade pitch angle. Li et al. [3] adopted an overset technique to simulate the aerodynamics of a wind turbine and investigate the effect of various wind speeds and pitch angles on the transient response of the machine.

In this work, a commercial 3-bladed rotor with a diameter of 100 m is modelled by an overset technique, together with its supporting structures, namely tower and nacelle. The whole machine is immersed in the ABL flow which leads to a wind speed increasing with height. Various operating points in the surrounding of the nominal operating point (NOP) are simulated by changing the pitch angle of the blades and the tip-speed ratio. Both the energy conversion performance of the turbine and the loads acting on the blades will be analysed in detail during the transient rotation of the machine.

2 METHODOLOGY

The domain of the flow simulation is displayed in fig. 1, with indication of the boundary conditions.

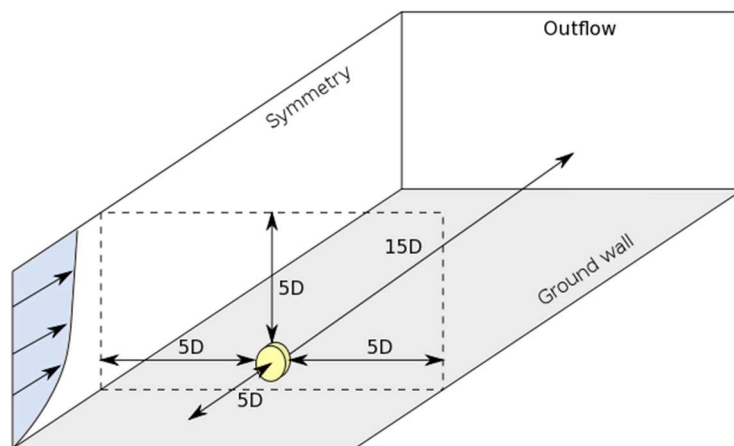


Figure 1: Simulation layout with the yellow cylinder denoting the domain around the rotor, with diameter D .

A distance equal to 5 rotor diameters from the top and side symmetry surfaces is chosen in order to avoid artificial acceleration of the flow. Furthermore, the inflow and the outflow are

respectively 5 and 15 rotor diameters away from the rotor.

A 3D fully hexahedral mesh is created for every component of the machine, namely the 3 blades, the hub, the nacelle and the tower. These meshes are then overlapped to a fully structured background mesh and connectivity is established by means of an overset technique [3, 4]. Fig. 2 shows the details of the mesh around each blade, while fig. 3 displays the background mesh and the mesh around tower and nacelle. In total, approximately 56 million cells are used.

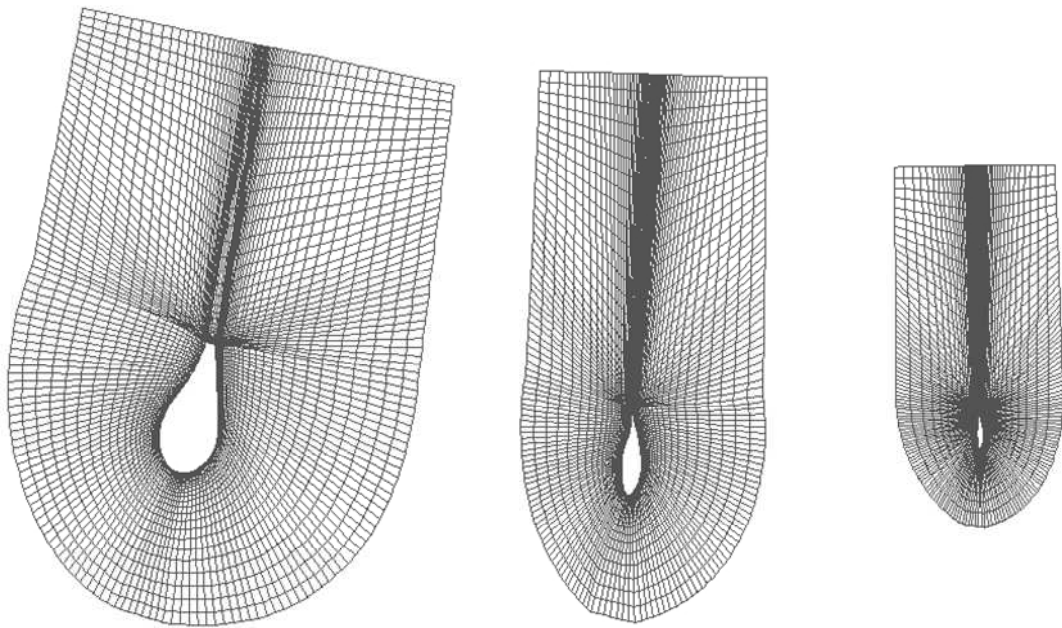


Figure 2: Sections of the component mesh around a blade: (left) 20% span, (center) 50% span, (right) 90% span.

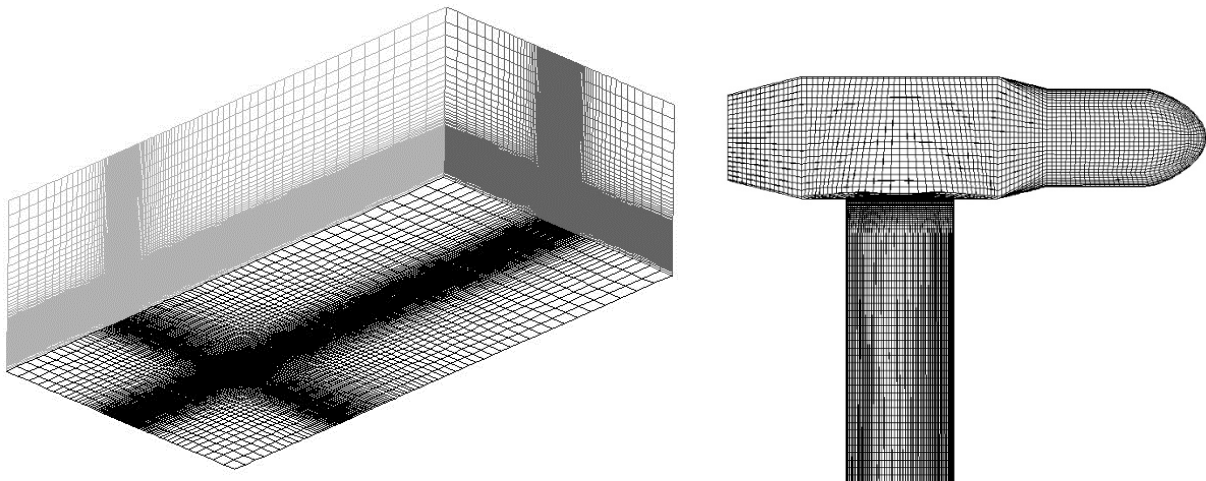


Figure 3: (left) background structured mesh and (right) detail of the mesh around tower and nacelle.

As an example of how the mesh connectivity is built, the connection of the blade mesh with the background grid is shown. The background cells encompassed or crossed by the blade walls

are deactivated. On the external boundary of the component mesh, the solution is obtained by interpolation from the background mesh. Here, the two meshes are designed to have roughly the same cell size. The (background) cells from where the solution is taken are marked as “donor cells”, while the (component) cells receiving solution by interpolation are marked as “receptor cells”. At least 4 donor cells contribute to interpolation on each receptor cell. This is summarized by fig. 4:

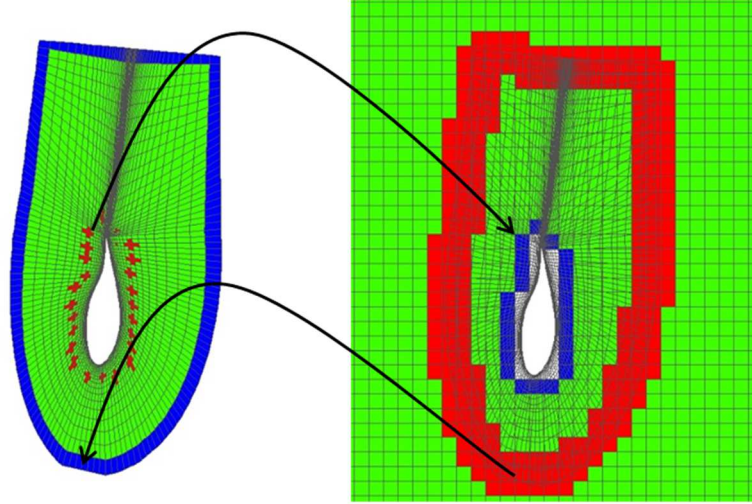


Figure 4: Mesh connectivity technique: (left) component mesh, (right) background and component mesh overlapped. Solve cells are marked in green, donor cells in red and receptor cells in blue.

The case is modelled as incompressible and turbulence is solved by means of the $k - \varepsilon$ model. At the inlet of the domain, the velocity, turbulent kinetic energy and dissipation rate distributions are prescribed to mimic the distribution of a neutral ABL. The profiles first proposed by Richard and Hoxey [5] are adopted. They are summarized hereunder:

$$u(z) = \frac{u_*}{K} \ln \left(\frac{z + z_0}{z_0} \right)$$

$$k = \frac{u_*^2}{\sqrt{C_\mu}}$$

$$\varepsilon(z) = \frac{u_*^3}{K(z + z_0)}$$

In these equations, u is the wind velocity as a function of the height z , u_* is the friction velocity (an index of the intensity of the wind), z_0 is the aerodynamic roughness length (which provides an estimation of the roughness of the ground wall) and k and ε are respectively the turbulent kinetic energy and its dissipation rate. Furthermore, K is the von Karman constant (0.4187) and C_μ is a constant of the turbulence model, set to 0.09. In order to consistently sustain and preserve the inlet profiles across the whole computational domain, a new formulation for the ground wall functions is necessary [6, 7, 8]. Thus, following the approach of Parente and Benocci [6], the aerodynamic roughness length is directly included in the wall functions, leading to a modified non-dimensional wall distance z^+ and a modified wall function constant E .

$$z_{mod}^+ = \frac{(z + z_0)u_*\rho}{\mu}$$

$$E_{mod} = \frac{\mu}{\rho z_0 u_*}$$

These modified wall functions are used on the ground wall (fig. 1), while the standard ones are used on every other wall.

In this work, the friction velocity is set to $u_* = 0.671082 \text{ m/s}$ and the aerodynamic roughness is set to $z_0 = 0.5 \text{ m}$, leading to a wind speed of 8.5 m/s at the hub height (100 m). The turbulent kinetic energy is set to $0.01512 \text{ m}^2/\text{s}^2$.

The momentum equations and continuity equation are solved together in a pressure-based solver. 2nd order upwind discretization for momentum is applied and a 1st order implicit scheme is used for time discretization.

The nominal operating point, as provided by the blade manufacturer, corresponds to a TSR of 8.5 and a pitch angle which is taken as reference and marked as “pitch 0°”. Around this point, 8 more points are analyzed, changing both the TSR and the pitch angle of the blades. The rotational speed of the turbine is changed in order to change its tip speed ratios, as summarized by table 1.

Table 1: Analyzed tip speed ratios and respective rotational speed

TSR	Rotational speed
7.5	1.275 rad/s
8.5	1.445 rad/s
9.5	1.615 rad/s

Independently of the TSR to be simulated, each full rotation of the wind turbine rotor is divided into 240 time steps. For each of these TSRs, 3 different blade pitch angles are simulated, being the pitch 0°, the pitch +2° and the pitch -2°. The last two are obtained by rotating the blades of +2° or -2° around their axis. This leads to a total of 9 simulations carried out.

First, the turbine rotation is started in the unperturbed ABL, considering a TSR of 8.5 for each analyzed pitch angle. Then, after 5 complete rotations, the TSR is changed to the desired value and additional full rotations (from 2 to 7) are carried out until the torque provided by the machine stabilizes (i.e. difference between the last two thirds of revolution smaller than 1.8%). Finally, only the last revolution is analyzed.

Running on 280 cores (10 nodes, each with 2 CPUs of the type 14-core Xeon E5-2680v4, 2.4GHz, inter-connected via InfiniBand), approximately one day is necessary to perform a complete revolution.

3 RESULTS

In this section, the energy conversion performance of the turbine in each of the simulated operating points will be analyzed, before examining the loads acting on each blade. The torque coefficient c_T and power coefficient c_P to be used, are defined as:

$$c_T = \frac{\text{Torque}}{\frac{1}{2}\rho v^2 AR}$$

$$c_P = \frac{\text{Power}}{\frac{1}{2}\rho v^3 A} = c_T \cdot TSR$$

where ρ is the constant density of air (1.225 kg/m^3), v is the undisturbed wind speed at the hub height (8.5 m/s), R the radius of the rotor (50 m) and A its frontal area. Furthermore, to define the position of each blade during the rotation, the azimuth angle will follow the logics illustrated by fig. 5.

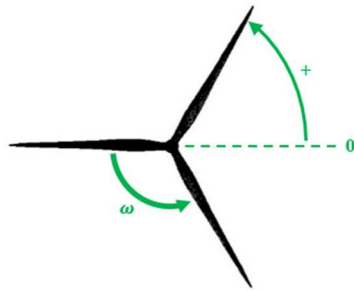


Figure 5: Definition of the blade azimuth angle.

For every operating point, qualitatively the same curve is observed for the torque during the last monitored revolution. Fig. 6 reports the total torque at the NOP, as a function of the azimuth angle of one of the three blades.

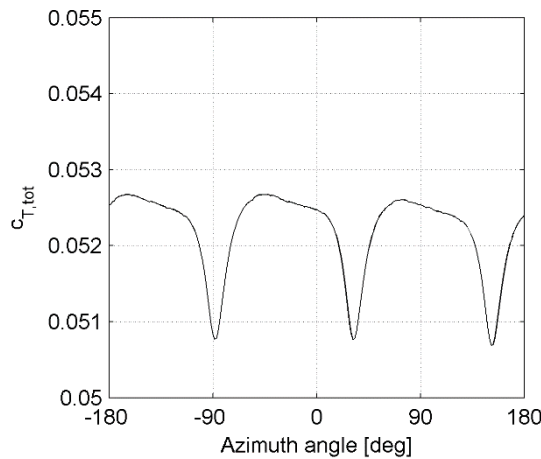


Figure 6: Total torque coefficient during the last revolution at NOP

The total torque coefficient exhibits a drop whenever a blade passes in front of the tower. This phenomenon is addressed as “tower dam” and results from the pressure increase induced by the tower obstruction on the suction side of the blade. It can be seen, in particular in fig. 7, showing the single blade contribution to the total torque provided by the turbine.

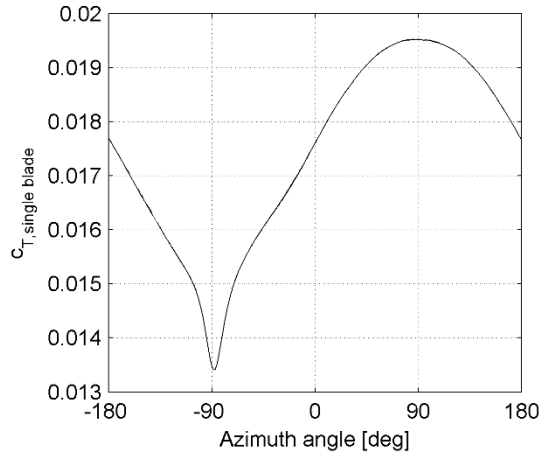


Figure 7: Single blade contribution to the torque during the last revolution at NOP

The single blade contribution has a large amplitude of oscillation (peak to peak amplitude being 35.7 % of the average value at NOP) due to the ABL. When the blade points upwards (i.e. positive azimuth angles) the wind speed is higher, which leads to higher angles of attack on the entire blade span. The opposite applies when the blade points downwards. Nevertheless, the total torque results from the sum of the 3 blades, and has a much more stable value (max deviation from the average value equal to 2.92 % of the average value). The same curves can be reported for every operating point with varying average value and amplitude. The average value of the total torque coefficient of each simulated point is summarized on the left hand side of fig. 8, while on the right hand side the peak to peak amplitude of the single blade contribution is displayed.

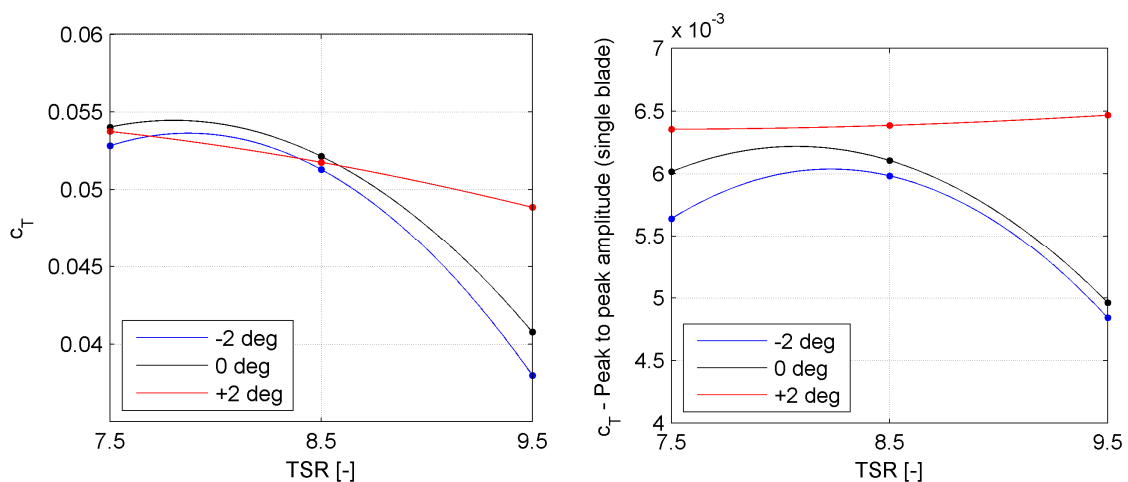


Figure 8: (left) Average values of total torque coefficient and (right) peak to peak amplitude of the single blade contribution.

Fig. 8 (right) shows that, for every pitch angle, an increase in TSR leads to a decrease in torque coefficient, since the angle of attack on the blade decreases. When the pitch angle is changed, the distribution of the angle of attacks over the entire blade span is shifted. This leads to a different operation of each airfoil lofted along the blade and, additionally, to different directions of the produced lift and drag forces. Consequently, the (positive) contribution of the lift and the (negative) contribution of the drag will combine differently to the produced torque, according to the adopted pitch angle and TSR.

Differently, the power produced by the turbine depends not only on the torque, but also on the rotational speed. Fig. 9 shows the average value of the power coefficient in every simulated operating point. When the TSR rises from 7.5 to 8.5, for two of the analyzed pitch angles (0° and -2°), the decay in the torque is compensated by a bigger increase in the rotational speed, leading to an overall higher power coefficient.

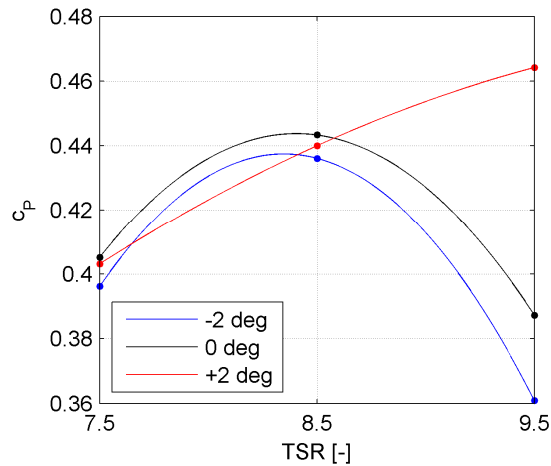


Figure 9: Average values of total power coefficient of the turbine.

It is also reported that the operating point corresponding to $+2^\circ$ pitch and 9.5 TSR has a higher power coefficient (+4.7 %) than the nominal operating point provided by the manufacturer, while every other operating point exhibits a lower coefficient (up to -18.6 % for -2° pitch and 9.5 TSR). It is useful to divide each blade into 20 equally spaced strips, as shown in fig. 10 and analyze how each strip contributes to the torque being provided by the single blade.

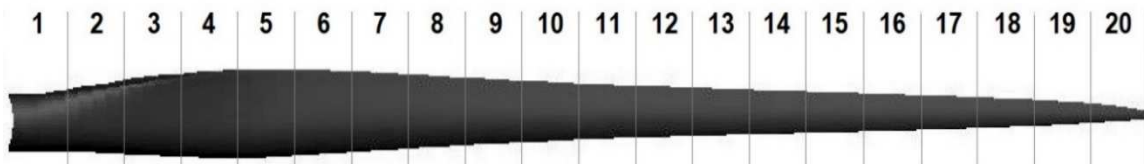


Figure 10: Blade strips.

Fig. 11 compares the torque and power coefficients per meter of blade provided when pointing upwards (i.e. blade azimuth angle of $+90^\circ$, when the contribution is maximal) at the

NOP and at the point with the highest power in fig. 8 (namely, $+2^\circ$ pitch angle and TSR equal to 9.5).

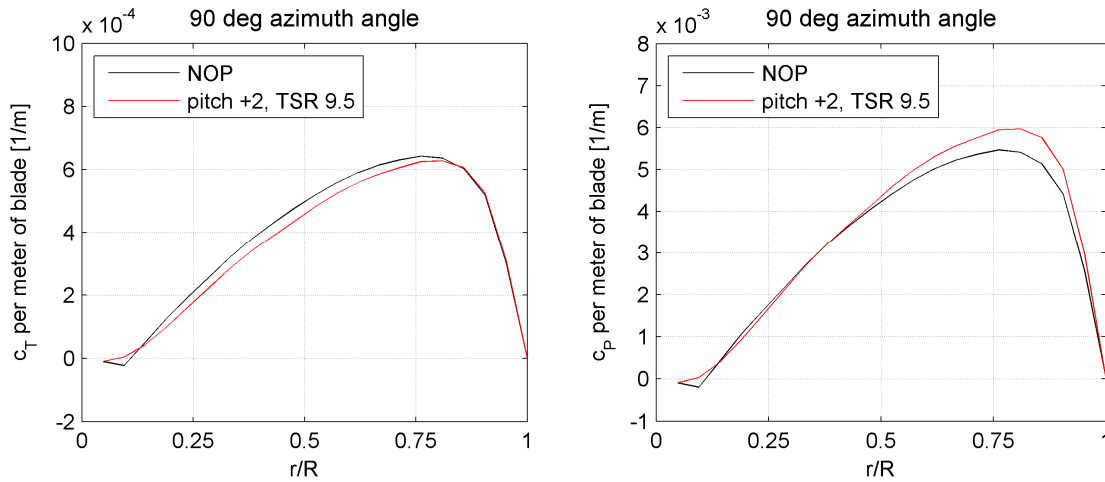


Figure 11: Distributions of (left) torque and (right) power coefficient per meter of blade as a function of the blade span, at 90° azimuth angle.

In these graphs, the area subtended on the abscissa corresponds to the torque and power coefficient of the blade. It can be noted that, over a large portion of the blade (below 75% of its span), the torque provided at the NOP is higher. By contrast, when examining the power coefficient, the distributions of the two operating points closely follow each other, except for a region of the blade located at about 75% of its span, where the NOP performs worse than the point corresponding to $+2^\circ$ pitch angle and 9.5 TSR. A similar condition is consistently reported during the whole rotation.

After examining how the performance of the machine changes with the operating point, a similar analysis can be carried out for the axial load acting on each blade. The axial force is in fact the highest force component and it is the one dominantly contributing to the deflection of the blades during the operation of the machine. Similarly to fig. 7, the axial force acting on each blade can be related directly to its position. At the NOP, the evolution of the axial force is depicted in fig. 12.

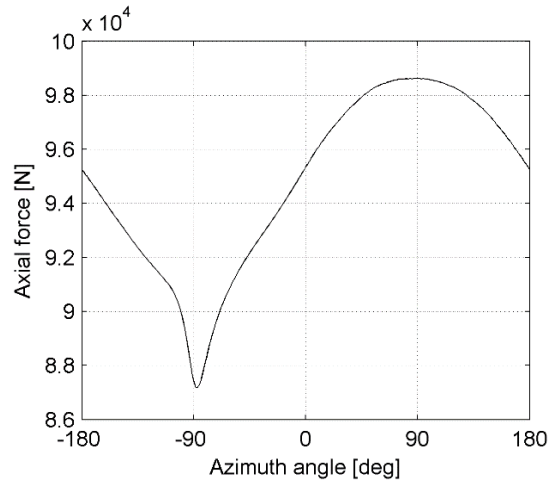


Figure 12: Axial force acting on the single blade as a function of its azimuth angle at NOP.

Similar curves can be reported for every simulated operating point. Both the effect of the ABL and the tower dam phenomenon are here clearly visible, similar to what was already reported for the torque in fig. 7. The average magnitude of the axial force acting on each blade is strongly dependent on the operating point, as shown in the left hand side of fig. 13.

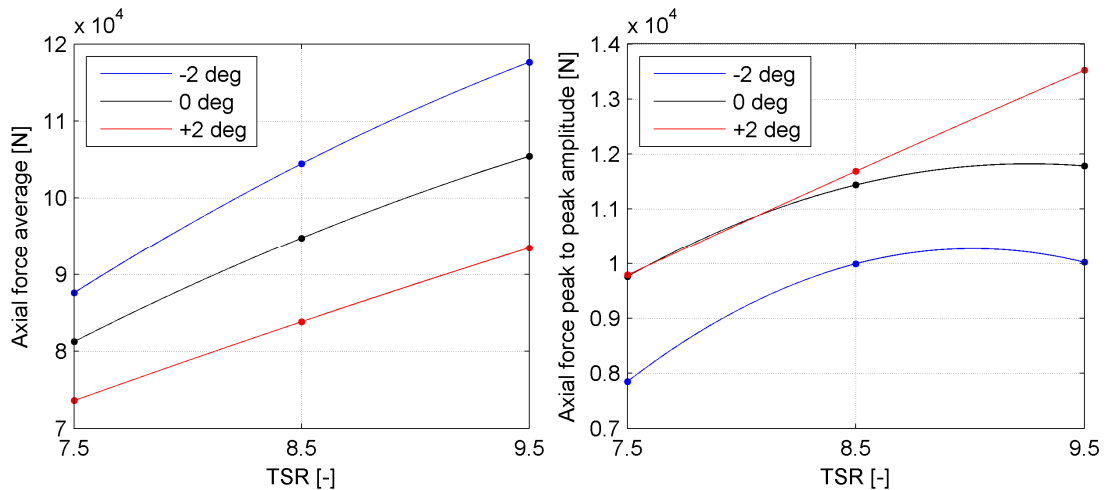


Figure 13: (left) Average values and (right) peak to peak amplitudes of the axial force acting on each blade.

In contrast to what has been observed for the power coefficient, the axial force average value shows an increasing trend when the TSR is increased, independent of the pitch angle. Furthermore, the curve is shifted down when the pitch angle of the blade is increased.

The point previously highlighted for having a higher c_p than the NOP also shows a slightly smaller average axial force (-1.7 %), but, at the same time, is also the one with the highest amplitude in its oscillation. The right hand side of fig. 13 shows how the peak to peak amplitude (difference between the highest value, reached at $+90^\circ$ and the lowest one, reached at -90°) is also largely affected by the operating point and it is connected to the arising of fatigue problems.

The operating point with -2° pitch and 9.5 TSR has the highest average value of the axial

force (+24.7 % when compared to NOP). The distribution of the axial force throughout the blade can also be analyzed as already done for the torque, leading to the graph in fig. 14.

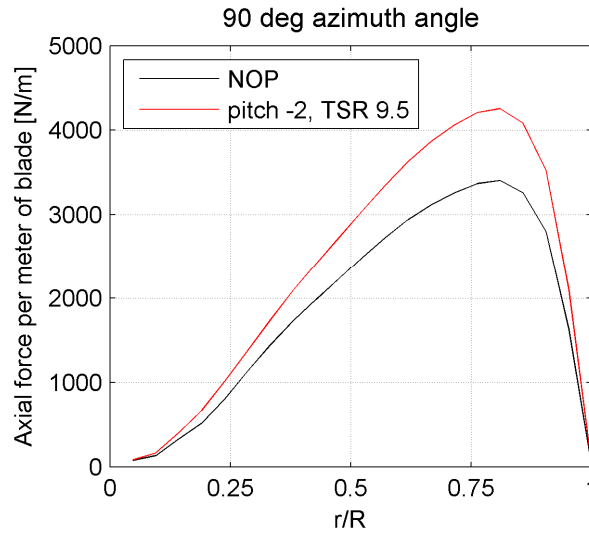


Figure 14: Distributions of axial force per meter of blade as a function of the blade span, at 90° azimuth angle.

A consistent increase of the axial force solicitation is monitored throughout the entire blade span and the highest increase is observed at about 75% of the radius, where the axial force also reaches its peak. A similar condition is reported during the entire rotation.

4 CONCLUSIONS

- Changing the blade pitch angle and its tip speed ratio, 9 operating points were simulated, keeping the ABL wind flow unchanged. In this way, the characteristic of the turbine has been built in the proximity of the nominal operating point (NOP). A better performing point could be identified and the different distribution of the power coefficient across the blade span showed how the improvement is mainly due to the blade part located around 75 % of its span.
- The axial force average value and amplitude of oscillation were also monitored, showing that the previously identified better performing point is characterized by a higher amplitude of the oscillating axial force on each blade. Furthermore, one of the operating points exhibited an average value of the axial force 24.7 % higher than at the NOP. This increase is spread over the entire blade span, being maximum at about 75 % of its span.

REFERENCES

- [1] E. Hau. “Wind Turbines: fundamentals, Technologies, Application, Economics” (2nd Edition). *Springer: Berlin*, 2006
- [2] A.R. Sudhamsu, M.C. Pandey et al. Numerical study of effect of pitch angle on performance characteristics of a HAWT. *Engineering Science and Technology, an International Journal*, 2016. DOI: 10.1016/j.jestch.2015.09.010
- [3] Y. Li, K.J. Paik, T. Xing, P. M. Carrica. Dynamic overset CFD simulations of wind turbine aerodynamics. *Renewable Energy*, 2012. DOI: 10.1016/j.renene.2011.06.029
- [4] F. Zahle, N.N. Sørensen and J. Johansen. Wind turbine rotor-tower interaction using an incompressible overset grid method. *Wind Energy* 2009. DOI:10.1002/we.327
- [5] P.J. Richards, R.P. Hoxey. Appropriate boundary conditions for computational wind engineering models using the k- ϵ turbulence model. *Journal of Wind Engineering and Industrial Aerodynamics*, **46 & 47**, 145-153, 1993.
- [6] A. Parente, C. Gorié, J. van Beeck, C. Benocci. A Comprehensive Modelling Approach for the Neutral Atmospheric Boundary Layer: Consistent Inflow Conditions, Wall Function and Turbulence Model. *Boundary Layer Meteorology*, 2011. DOI 10.1007/s10546-011-9621-5
- [7] B. Blocken, T. Stathopoulos, J. Carmeliet. CFD simulation of the atmospheric boundary layer: wall function problems. *Atmospheric Environment*, 2017. DOI: 10.1016/j.atmosenv.2006.08.019
- [8] A. Parente, C. Gorié, J. van Beeck, C. Benocci. Improved k- ϵ model and wall function formulation for the RANS simulation of ABL flows. *Journal of Wind Engineering and Industrial Aerodynamics*, 2011. DOI: 10.1016/j.jweia.2010.12.017